

Ruling out AGNs as the dominant source of cosmic reionization with JWST

Danyang Jiang^{1,2}, Linhua Jiang^{1,2}, Shengxiu Sun^{1,2}, Weiyang Liu^{1,2}, and Shuqi Fu^{1,2}

¹Department of Astronomy, School of Physics, Peking University, Beijing 100871, China

²Kavli Institute for Astronomy and Astrophysics, Peking University, Beijing 100871, China

Cosmic reionization represents the latest phase transition of the intergalactic medium (IGM) in the Universe. It has long been debated whether galaxies or active galactic nuclei (AGNs) are the major source of Lyman continuum (LyC) photons responsible for reionization. Previous observations slightly favored galaxies as the major ionizing source^{1,2,3}. However, the James Webb Space Telescope (JWST) recently discovered an unexpectedly high density of AGN candidates at high redshift, which has largely enhanced the influence of AGNs^{4,5,6,7,8,9,10,11,12}. Here we derive a definitive upper bound on the AGN contribution to reionization using the latest JWST data, and conclusively rule out AGNs as the dominant ionizing source during the epoch of reionization (EoR). We build a sample of objects (including galaxies and AGNs) in a specific redshift range between 7.15 and 7.75 that has a high completeness. Each object is then decomposed into a point-source component and an extended component in their rest-frame far-UV JWST images. Assuming all point-source components are AGNs, we obtain an absolute upper limit for the density of the AGN population. This fiducial AGN sample reaches an unprecedentedly low luminosity of $M_{UV} \approx -15$ mag. Based on this sample, we find that AGNs can contribute at most one third of the LyC photons required to ionize the Universe in this redshift range. Our result implies that galaxies dominate the ionizing source during the EoR.

The major source of LyC photons responsible for cosmic reionization remains controversial, because the individual contributions of the two main sources, galaxies (or stars) and AGNs (or supermassive black holes), are not well constrained^{13,14,15}. JWST is revolutionizing our understanding of reionization by routinely finding high-redshift ($z \geq 6$) galaxies and AGNs. It is found that galaxies can produce sufficient LyC photons if their escape fraction f_{esc} is higher than $10 \sim 15\%$ (ref.^{16,17}). However, the average f_{esc} value of lower-redshift galaxies is only a few percent^{18,19}, and it is unrealistic to directly detect the LyC emission from high-redshift objects due to the IGM absorption. On the other hand, the UV luminosity function (LF) of luminous AGNs (i.e., quasars) has been well established^{1,3}. Despite that the faint end of the AGN LF is very uncertain, previous studies suggest that the AGN contribution to reionization is small^{1,2,3}. Recently, JWST discovered a large number of faint AGN candidates at $z \geq 4$ (ref.^{4,5,6,7,8,9,10,11}), including the so-called ‘little-red-dots’ (LRDs) whose nature is still unclear^{20,21,22}. If the majority of these objects are AGNs, the AGN spatial density at the faint end would be hundreds of times higher than the extrapolated value from the current AGN LF^{5,7,8,9}. This leads to a possibility that AGNs play an important role on producing ionizing photons.

In this work we derive the absolute upper bound of the AGN contribution to reionization without knowing the nature of LRDs (and galaxies in general). We first build a sample of objects at $7.15 \leq z \leq 7.75$, including galaxies and AGNs, using JWST images in the GOODS (GOODS-S and GOODS-N) fields. This redshift range covers the peak of cosmic reionization²³. It is optimal for our target selection, because the strong Ly α break caused by the IGM absorption produces very red F090W – F115W colors, which is highly efficient to remove low-redshift contaminants. Figure 1 demonstrates our color selection using a composite quasar spectrum². Each of the selected object is then decomposed into a point-source component and an extended component using the JWST images. Hereafter we assume that all point-

source components are AGNs, and thus set an absolute upper bound for the AGN population. With this assumption, we calculate the AGN UV LF and measure the ionizing photons produced by AGNs. We adopt a standard Λ CDM cosmology with $H_0 = 70 \text{ km s}^{-1} \text{ Mpc}^{-1}$, $\Omega_m = 0.3$, and $\Omega_\Lambda = 0.7$. All magnitudes are in the AB system.

We select our high-redshift sample in two steps. We first use the photometric catalog of the GOODS fields provided by the JWST Advanced Deep Extragalactic Survey (JADES) program^{24,25,26} to select objects in the required redshift range. This produces a preliminary sample. In the second step we refine the sample using the F090W – F115W color. We download all JWST NIRCcam images in the GOODS fields from the MAST archive and make our own combined images (see Methods for details). Our images are deeper than those from the JADES public release because we include images taken by other programs. The depth (5σ detection within a $0''.24$ circular diameter) of the F115W-band images reach ~ 29.2 mag in GOODS-N and ~ 30.1 mag in GOODS-S. We perform the aperture photometry of the selected objects in the F090W and F115W images. To refine the preliminary sample, we implement the following two criteria: 1) detection significance $> 7\sigma$ in F115W (the primary detection band), and 2) F090W – F115W > 2 (or detection significance $< 2\sigma$ in F090W). All objects are visually inspected. Finally, we obtain a sample of 156 objects, including 109 in GOODS-S and 47 in GOODS-N. The areas of the GOODS-S and GOODS-N fields that we use are 67.0 arcmin^2 and 56.4 arcmin^2 , respectively.

We perform the image decomposition²⁷ of the 156 objects using high-resolution JWST images in two rest-frame far-UV bands F115W and F150W (Methods). The decomposition model consists of a point spread function (PSF) and a Sérsic profile for AGN and galaxy components, respectively. Figure 2 illustrates our image decomposition with two examples. AGN fraction is defined for each object as the ratio of the PSF flux to the total flux, and its typical measurement uncertainty is 5%. Figure 3 shows the AGN fractions of the sample. We select sources with AGN fractions higher than 20% in F115W and F150W, i.e., we require that the significance of the AGN detection is higher than 4σ . Objects with lower fractions are completely dominated by galaxies and thus contribute little to the AGN population. Our final AGN sample contains 93 AGNs, including 65 in GOODS-S and 28 in GOODS-N. We compute their UV magnitudes at rest-frame 1450\AA (M_{1450}) using the decomposed PSF flux (Methods). They span a very low luminosity range $-15 \leq M_{1450} \leq -20$ mag.

We cross match the parent sample of the 156 objects with known LRD candidates in the same regions^{7,8,11}, and find that the sample covers two known LRDs. The other LRDs are either out of the desired redshift range or too faint in the UV band. We further find that our final AGN sample covers one of the two LRDs. The other one is excluded because its AGN fraction is below 20%. Note that LRDs are primarily identified using rest-frame optical images, and they can be very faint and extended in the rest-frame UV, which is confirmed by the above finding. Therefore, a high spatial density of LRDs does not mean a correspondingly high production rate of UV photons.

We measure the AGN UV LF using the above sample. We first perform simulations to estimate our sample completeness by computing a selection function, i.e., the probability that a galaxy hosting an AGN with a given magnitude M_{1450} at a given redshift z can be selected by our target selection procedure (Methods). We generate two simulated spectral samples for AGN and galaxy components, based on the observed distribution of AGN fractions in the F115W band. The AGN SED model is the same as the quasar model used for our M_{1450} measurement. The galaxy SED is modeled as a power-law continuum, with a slope randomly drawn from a Gaussian distribution based on an empirical relation between UV-continuum slope and UV magnitude of $z \sim 7$ galaxies²⁸. The total F090W and F115W magnitudes are then measured from the AGN and galaxy model spectra. With the simulated magnitudes, we add photometric errors for each survey region and calculate the selection function using the standard procedure^{1,29} (Methods).

We compute the binned UV LF using the traditional $1/V_a$ method³⁰. The available cosmic vol-

ume for an AGN with M_{1450} and z in a magnitude bin ΔM_{1450} and a redshift bin Δz is given by $V_a = \int_{\Delta M_{1450}} \int_{\Delta z} p(M_{1450}, z) \frac{dV}{dz} dz dM_{1450}$, where the $p(M_{1450}, z)$ is the selection function derived above. The binned LF is $\Phi(M_{1450}, z) = \sum 1/V_a^i$, where the sum is over all AGNs in the sample. The uncertainty of the binned LF is the quadrature sum of the Poisson error and the error originated from cosmic variance. We ignore the redshift evolution of the LF over the measured redshift range ($7.15 \leq z \leq 7.75$). The redshift bin size is $\Delta M_{1450} = 0.7$, except for the low and high luminosity ends where the sample sizes are small. The calculated binned LF is presented as the red circles in Figure 4a.

We further parametrize the LF using a double power-law (DPL) with four parameters, including the faint-end slope α , bright-end slope β , characteristic magnitude M_{1450}^* , and normalization factor Φ^* . Since our sample only covers low-luminosity AGNs and the bright end of the LF has been well determined, we fix the bright end slope β to be -2.78 from the literature³¹. We use a maximum likelihood function³² and perform a Markov Chain Monte Carlo (MCMC) analysis³³ to determine the best fits of two free parameters α and M_{1450}^* . The results are $\alpha = -1.70_{-0.25}^{+0.44}$ and $M_{1450}^* = -17.81_{-1.35}^{+1.06}$ mag. The 1σ uncertainties reported here are derived from the 16th and 84th percentiles of the MCMC parameter distributions. The associated Φ^* is $10^{-3.7} \text{ Gpc}^{-3} \text{ mag}^{-1}$. Because of the high density at the faint end, the LF does not show a distinct ‘knee’. Therefore, M_{1450}^* has relatively large errors, which has negligible impact on our following calculation. Figure 4a shows our LF compared with the LFs of quasars, LRDs, and galaxies from the literature^{2,8,31,34}. Our AGN LF is approximately a few thousand times higher than the extrapolation of the bright quasar LF³¹, tens of times lower than the galaxy LF³⁴, and slightly higher than the upper limit of faint AGN LF² based on the observational data before JWST.

We follow standard methods^{1,29} to calculate the density of ionizing photons produced by AGNs using the above AGN LF. To estimate the number of ionizing photons from an AGN, we assume that the escape fraction of ionizing photons is 100%, and use a broken power-law SED³⁵ around 912\AA : $f_\nu \propto \nu^{-0.61}$ at wavelength $\lambda > 912\text{\AA}$ and $f_\nu \propto \nu^{-1.70}$ at $\lambda < 912\text{\AA}$, where ν is frequency. We integrate this SED over an energy range of 1–4 Ryd. We then integrate the AGN LF over a luminosity range from $M_{1450} = -30$ to -15 mag to obtain the total ionizing photons from the AGN population. The result is compared with the total ionizing photon emissivity per unit comoving volume required to ionize the Universe, which is $\dot{N}_{\text{ion}}(z) = 10^{50.48} (\frac{C}{3}) \times (\frac{1+z}{7})^3 \text{ Mpc}^{-3} \text{ s}^{-1}$ (ref.³⁶), where C is the IGM clumping factor and we adopt a typical value 3 (ref.³⁷). In the calculation we have assumed the baryon density of $\Omega_b h^2 = 0.022$. We define a fraction f_{AGN} as the ratio of the total observed AGN emissivity to the total required photon emissivity, and the result from the above calculations is $f_{\text{AGN}} = 33_{-4}^{+6}\%$. Figure 4b illustrates the cumulative f_{AGN} as a function of luminosity, and shows that low-luminosity AGNs dominate f_{AGN} .

The resultant $f_{\text{AGN}} = 33\%$ effectively rules out the AGN-dominant scenario for cosmic reionization. We emphasize that this value is the absolute upper bound for two main reasons. One is that the escape fraction of ionizing photons from AGNs has been assumed to be 100%. This is a reasonable approximation for luminous quasars³⁸, but should be smaller in low-luminosity AGNs^{39,40,41}. If it is lower than 100%, f_{AGN} would decrease accordingly. The second reason is the assumption during the image decomposition procedure. We have assumed that the PSF component is entirely from AGN. This ignores the flux from a possible compact galaxy core and overestimates the AGN flux. Some galaxies are very compact and PSF-like even in JWST images^{22,42}. Our result concludes a subdominant role of AGNs for reionizing the Universe. It implies that star-forming galaxies provide most ionizing photons. Future JWST observations may find solid evidence supporting the dominant role of galaxies.

Figures

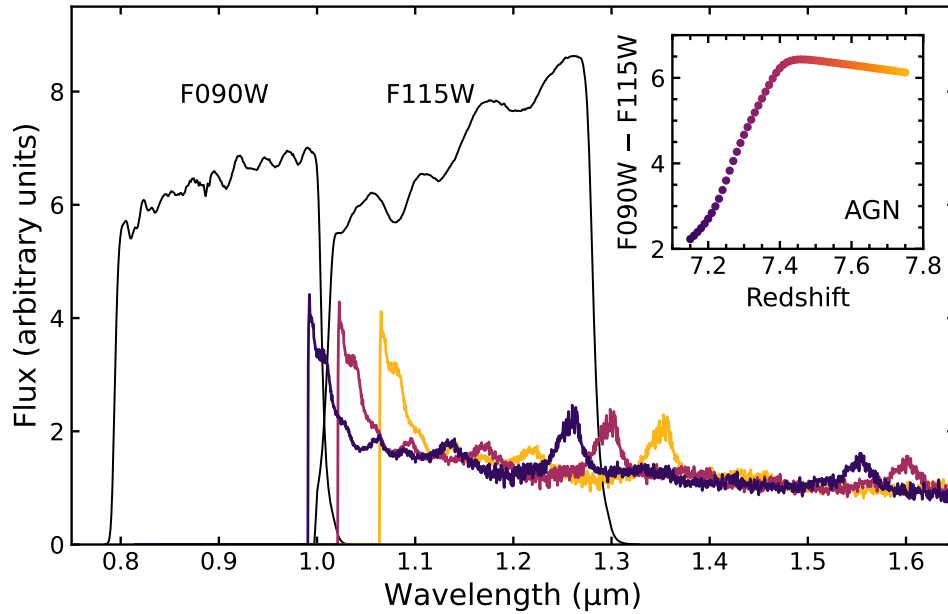


Figure 1. Color selection of high-redshift AGNs. The three spectra represent a composed spectrum of $z \sim 6$ quasars (AGNs) from ref. ² that has been redshifted to $z = 7.15, 7.40,$ and $7.75,$ respectively. We have assumed that the spectra blueward of $\text{Ly}\alpha$ have been completely absorbed by the IGM. The two black filter transmission curves represent JWST F090W and F115W filters. The inset shows how the F090W–F115W color changes with redshift. We use $F090W - F115W > 2$ to select high-redshift sources at $z = 7.15 - 7.75.$

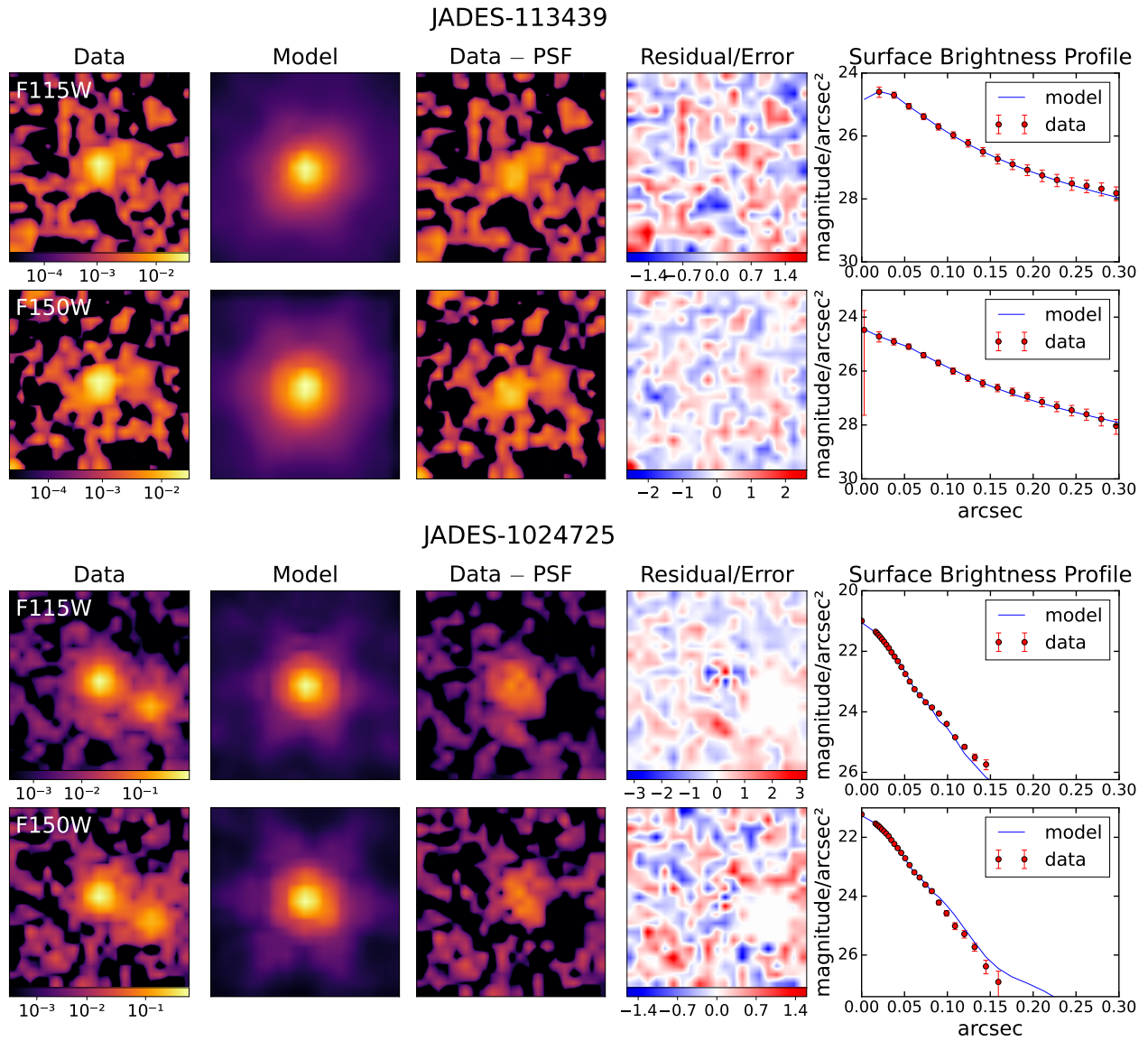


Figure 2. Two examples of JWST image decomposition in the F115W and F150W bands. The AGN fractions in the two cases are $\sim 40\%$ and $\sim 70\%$, respectively. The size of each image is 21 pixels (0.63 arc-seconds) on a side, centered on the flux peaks of the targets. The five columns from left to right display the following information: (1) the observed JWST image; (2) the best-fit model consisting of a point source (PSF) plus a Sérsic host galaxy; (3) the PSF-subtracted image; (4) the fitting residual image divided by the error image; (5) the surface brightness profile. The color maps reflect the flux level in the unit of counts per second on a logarithmic scale, as shown by the attached color bars. This image decomposition procedure works well for our sample.

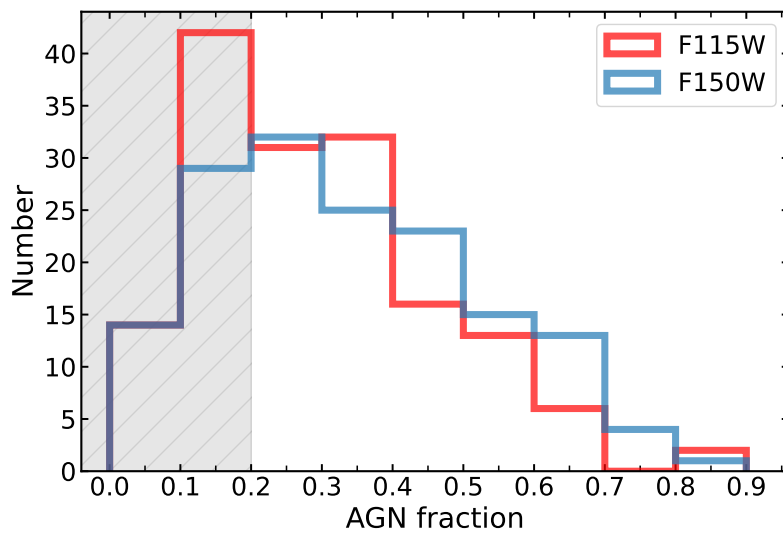


Figure 3. AGN fractions in the F115W and F150W bands. The histograms show the AGN fractions for our sample of 156 high-redshift objects in F115W and F150W. The shaded region represents AGN fractions below 20%, and AGNs in this region are excluded from our final AGN sample. The two distributions are generally consistent.

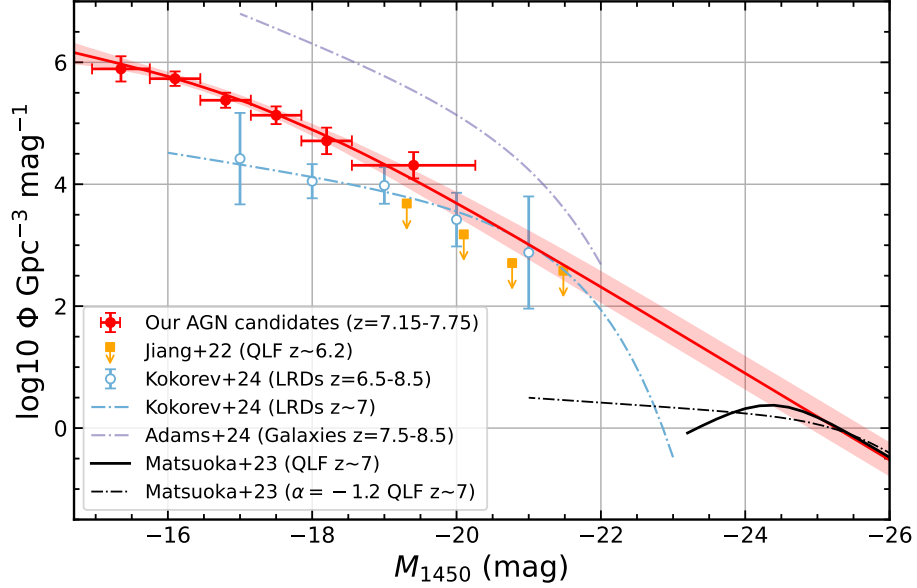
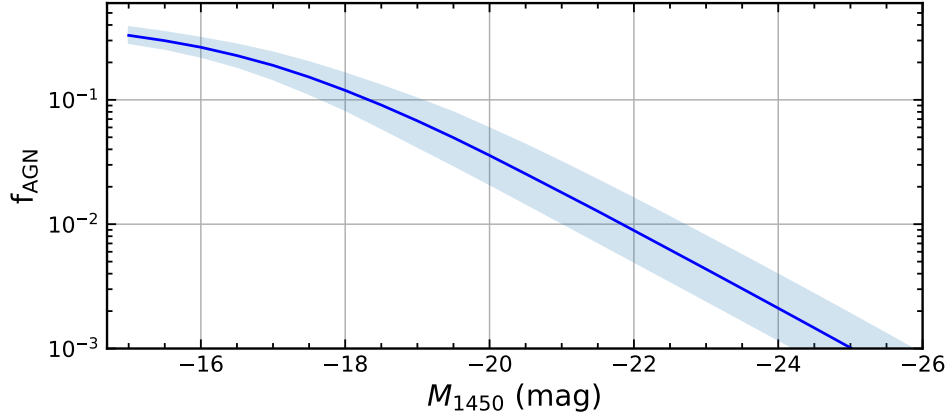
a**b**

Figure 4. AGN UV LF and the upper limit of the AGN contribution to reionization. **a**, UV LF at redshift $z = 7.15 - 7.75$. The red circles represent our binned LF. Its horizontal bars indicate the luminosity ranges covered by the bins and the vertical bars show the 1σ errors of the LF. The solid red line with the shaded region represents our best-fit DPL LF with its 1σ region. The light purple dot-dashed line represents a galaxy LF at $z = 7.5 - 8.5$ from ref. ³⁴. The black solid line and black dot-dashed line represent two bright quasar LFs (QLF) at $z \sim 7$ from ref. ³¹ with a free and a fixed faint-end slope, respectively. The filled orange squares represent the upper limit of AGN LF at $z \sim 6.2$ from ref. ² based on the observational data before JWST. The light blue open circles and dot-dashed line represent the LRDs LF from ref. ⁸. **b**, Upper limit of the AGN contribution to reionization. The solid blue curve with its $\pm 1\sigma$ uncertainty region represents the cumulative fraction (f_{AGN}) of the AGN emissivity to the total photon emissivity required to ionize the Universe. They are computed using the above LF. This result excludes the AGN-dominant scenario for cosmic reionization.

References

1. Matsuoka, Yoshiki et al. Subaru High- z Exploration of Low-luminosity Quasars (SHELLQs). V. Quasar Luminosity Function and Contribution to Cosmic Reionization at $z = 6$ *Astrophys. J.* **869**, 150 (2018).
2. Jiang, Linhua et al. Definitive Upper Bound on the Negligible Contribution of Quasars to Cosmic Reionization *Nat. Astron.* **6**, 850–856 (2022).
3. Schindler, Jan-Torge et al. The Pan-STARRS1 $z > 5.6$ Quasar Survey. III. The $z \approx 6$ Quasar Luminosity Function *Astrophys. J.* **943**, 67 (2023).
4. Onoue, Masafusa et al. A Candidate for the Least-massive Black Hole in the First 1.1 Billion Years of the Universe *Astrophys. J. Lett.* **942**, L17 (2023).
5. Harikane, Yuichi et al. A JWST/NIRSpec First Census of Broad-line AGNs at $z = 4–7$ *Astrophys. J.* **959**, 39 (2023).
6. Kocevski, Dale D. et al. Hidden Little Monsters: Spectroscopic Identification of Low-mass, Broad-line AGNs at $z > 5$ with CEERS *Astrophys. J. Lett.* **954**, L4 (2023).
7. Kocevski, Dale D. et al. The Rise of Faint, Red AGN at $z > 4$: A Sample of Little Red Dots in the JWST Extragalactic Legacy Fields *arXiv e-prints* (2024).
8. Kokorev, Vasily et al. A Census of Photometrically Selected Little Red Dots at $4 < z < 9$ in JWST Blank Fields *Astrophys. J.* **968**, 38 (2024).
9. Matthee, Jorryt et al. Little Red Dots: An Abundant Population of Faint Active Galactic Nuclei at $z \sim 5$ Revealed by the EIGER and FRESCO JWST Surveys *Astrophys. J.* **963**, 129 (2024).
10. Greene, Jenny E. et al. UNCOVER Spectroscopy Confirms the Surprising Ubiquity of Active Galactic Nuclei in Red Sources at $z > 5$ *Astrophys. J.* **964**, 39 (2024).
11. Williams, Christina C. et al. The Galaxies Missed by Hubble and ALMA: The Contribution of Extremely Red Galaxies to the Cosmic Census at $3 < z < 8$ *Astrophys. J.* **968**, 34 (2024).
12. Piero Madau et al. Cosmic Reionization in the JWST Era: Back to AGNs? *Astrophys. J. Suppl. Ser.* **971**, 75 (2024).
13. Miralda-Escudé et al. Reionization of the Inhomogeneous Universe *Astrophys. J.* **530**, 1 (2000).
14. Volonteri, Marta et al. RELATIVE ROLE OF STARS AND QUASARS IN COSMIC REIONIZATION *Astrophys. J.* **703**, 2113 (2009).
15. Onoue, Masafusa et al. Minor Contribution of Quasars to Ionizing Photon Budget at $z \sim 6$: Update on Quasar Luminosity Function at the Faint End with Subaru/Suprime-Cam *Astrophys. J. Lett.* **847**, L15 (2017).
16. Mascia, S. et al. New Insight on the Nature of Cosmic Reionizers from the CEERS Survey *Astron. Astrophys.* **685**, A3 (2024).

17. Lily Whitler et al. The $z \gtrsim 9$ galaxy UV luminosity function from the JWST Advanced Deep Extragalactic Survey: insights into early galaxy evolution and reionization *arXiv e-prints* (2024).
18. Grazian, A. et al. Lyman Continuum Escape Fraction of Faint Galaxies at $z \sim 3.3$ in the CANDELS/GOODS-North, EGS, and COSMOS Fields with LBC *Astron. Astrophys.* **602**, A18 (2017).
19. Liu, Yuchen et al. Lyman Continuum Emission from Spectroscopically Confirmed Ly α Emitters at $z \sim 3.1$ *Astrophys. J.* **958**, 22 (2023).
20. Li, Zhengrong et al. Little Red Dots: Rapidly Growing Black Holes Reddened by Extended Dusty Flows *arXiv e-prints* (2024)
21. Zhang, Zijian et al. Analysis of Multi-epoch JWST Images of ~ 300 Little Red Dots: Tentative Detection of Variability in a Minority of Sources *arXiv e-prints* (2024)
22. Labbe, Ivo et al. An Unambiguous AGN and a Balmer Break in an Ultraluminous Little Red Dot at $Z=4.47$ from Ultradeep UNCOVER and All the Little Things Spectroscopy *arXiv e-prints* (2024)
23. Collaboration, Planck et al. Planck 2018 Results. VI. Cosmological Parameters *Astron. Astrophys.* **641**, A6 (2020).
24. Rieke, Marcia J. et al. JADES Initial Data Release for the Hubble Ultra Deep Field: Revealing the Faint Infrared Sky with Deep JWST NIRC*am* Imaging *Astrophys. J. Suppl. Ser.* **269**, 16 (2023).
25. Eisenstein, Daniel J. et al. The JADES Origins Field: A New JWST Deep Field in the JADES Second NIRC*am* Data Release *arXiv e-prints* (2023).
26. D'Eugenio, Francesco et al. JADES Data Release 3 – NIRSpec/MSA Spectroscopy for 4,000 Galaxies in the GOODS Fields *arXiv e-prints* (2024).
27. Zhuang, Ming-Yang et al. Evolutionary Paths of Active Galactic Nuclei and Their Host Galaxies *Nat. Astron.* **7**, 1376–1389 (2023).
28. Bouwens, R. J. et al. UV-CONTINUUM SLOPES OF >4000 $z \sim 4-8$ GALAXIES FROM THE HUDF/XDF, HUDF09, ERS, CANDELS-SOUTH, AND CANDELS-NORTH FIELDS *Astrophys. J.* **793**, 115 (2014).
29. Jiang, L. et al. The final SDSS high-redshift quasar sample of 52 quasars at $z > 5.7$. *Astrophys. J.* **833**, 222–238 (2016).
30. Avni, Y. et al. On the Simultaneous Analysis of Several Complete Samples. The V/V_{\max} and V_e/V_a Variables, with Applications to Quasars. *Astrophys. J.* **235**, 694-716 (1980).
31. Matsuoka, Yoshiki et al. Quasar Luminosity Function at $z = 7$ *Astrophys. J. Lett.* **949**, L42 (2023).
32. Marshall, H. L. et al. Analysis of Complete Quasar Samples to Obtain Parameters of Luminosity and Evolution Functions *Astrophys. J.* **269**, L35-41 (1983).
33. Foreman-Mackey, Daniel et al. Emcee: The MCMC Hammer *Publ. Astron. Soc. Pacific* **125**, 306 (2013).

34. Adams, Nathan J. et al. EPOCHS. II. The Ultraviolet Luminosity Function from $7.5 < z < 13.5$ Using 180 Arcmin² of Deep, Blank Fields from the PEARLS Survey and Public JWST Data *Astrophys. J.* **965**, 169 (2024).
35. Lusso, E. et al. The First Ultraviolet Quasar-Stacked Spectrum at $z \simeq 2.4$ from WFC3 *Mon. Not. R. Astron. Soc.* **449**, 4204–4220 (2015).
36. Madau, Piero et al. Radiative Transfer in a Clumpy Universe. III. The Nature of Cosmological Ionizing Sources *Astrophys. J.* **514**, 648 (1999).
37. Finlator, Kristian et al. Gas Clumping in Self-Consistent Reionization Models *Mon. Not. R. Astron. Soc.* **427**, 2464–2479 (2012).
38. Cristiani, Stefano et al. The Spectral Slope and Escape Fraction of Bright Quasars at $z \sim 3.8$: The Contribution to the Cosmic UV Background *Mon. Not. R. Astron. Soc.* **462**, 2478–2485 (2016).
39. Micheva, Genoveva et al. Lyman Continuum Leaking AGN in the SSA22 Field *Mon. Not. R. Astron. Soc.* **465**, 302–315 (2017).
40. Grazian, A. et al. The Contribution of Faint AGNs to the Ionizing Background at $z \sim 4$ *Astron. Astrophys.* **613**, 0004–6361 (2018).
41. Iwata, Ikuru et al. Ionizing Radiation from AGNs at $z > 3.3$ with the Subaru Hyper Suprime-Cam Survey and the CFHT Large Area U-band Deep Survey (CLAUDS) *Mon. Not. R. Astron. Soc.* **509**, 1820–1836 (2022).
42. Pérez-González, Pablo G. et al. What Is the Nature of Little Red Dots and What Is Not, MIRI SMILES Edition *Astrophys. J.* **968**, 4 (2024)
43. Simmonds, C. et al. Ionising Properties of Galaxies in JADES for a Stellar Mass Complete Sample: Resolving the Cosmic Ionising Photon Budget Crisis at the Epoch of Reionisation *arXiv e-prints* (2024).

Acknowledgements

We acknowledge support from the National Key R&D Program of China (2022YFF0503401) and the National Science Foundation of China (12225301).

Author Contributions

D.J. analyzed the data, performed the calculations, and wrote the manuscript. L.J. designed program and wrote the manuscript. S.S. helped with the image decomposition. W.L. performed the JWST NIRCам image data reduction. S.F. helped with the target selection. S.S., W.L., and S.F. all contributed to the relevant sections of the manuscript.

Data Availability

All JWST data used in this paper are publicly available in the MAST archive.

Code Availability

Data were reduced using publicly available data reduction pipelines. Public tools were used for data analysis: SEP⁴⁵, GalfitM⁴⁹, statmorph⁵⁰, photutils⁵¹.

Competing interests

The authors declare that they have no competing interests.

Correspondence

Correspondence and requests for materials should be addressed to L.J (linhua.jiang@pku.edu.cn).

Methods

JWST NIRC*am* image reduction. We used raw JWST/NIRC*am* image files `uncal.fits` in the GOODS-S and GOODS-N fields from the MAST archive. The images in the GOODS-S field are from proposal ID 1180, 1210, 1283, 1286, 1895, 1963, 2079, 2198, 2514, 3215, 3990, and 6541, and the images in the GOODS-N field are from proposal ID 1181, 1895, 2514, 2674, and 3577. We reduced the data using the combination of the JWST Calibration Pipeline (v.1.12.5), the scripts for CEERS NIRC*am* imaging reduction¹, and our own custom codes. The details of the CEERS pipeline are presented in ref. ⁴⁴. Here we provide a brief description of the steps for our image reduction.

Stage 1 of the JWST Calibration Pipeline performed detector-level corrections, starting from `uncal.fits` files and ending with `rate.fits` files in units of count per second. Before running the ramp-fitting step in Stage 1 of the pipeline, we identified snowballs, enlarged their footprints, and flagged them as the `JUMP_DET` so that snowballs were properly removed after the ramp-fitting step. “Wisp” features from detector B4 of the F150W, F200W, and F210M images were subtracted using the wisp templates provided by the NIRC*am* team². The horizontal and vertical striping patterns (i.e., $1/f$ noise) in the images, were subtracted with `remstriping.py` in the CEERS team’s scripts.

We ran Stage 2 of the JWST Calibration Pipeline with the default parameters, which involve individual image calibrations such as flat-fielding and flux calibration. The output files are `cal.fits`. We ran Stage 3 of the JWST Calibration Pipeline to obtain a single mosaic for each filter in each field. The astrometry was calibrated using `TweakregStep` with user-provided reference catalogs that were produced as follows. We first generated a WCS reference catalog using the Hubble Legacy Field GOODS-S/GOODS-N F814W image. We then registered JWST long-wavelength (LW) F277W, F356W, F410M, and F444W images using the F814W WCS. All these LW images were combined to make a master image. Finally, a reference catalog was produced by detecting objects in this master image.

After running `SkyMatchStep` and `OutlierDetectionStep`, we subtracted a 2D background for each image following the method described in ref. ⁴⁴ and ran `ResampleStep` to drizzle and combine images to make one mosaic per filter. We set `pixfrac` to 0.8 and pixel scale to $0''.03$ for all filters. The `output_shape`, the `CRVAL`, and the `CRPIX` parameters are the same for each field so that the mosaics of all filters have the same WCS grid. Finally, a 2D background was subtracted from each mosaic using the method described in ref. ⁴⁴.

High-redshift sample selection. We built our sample at $7.15 \leq z \leq 7.75$. In this redshift range, the strong Ly α break in object spectra results in a very red F090W – F115W color that can efficiently distinguish high-redshift quasars and galaxies from lower-redshift objects. Because the sky coverage of JWST F070W images in the GOODS fields is small and the F115W – F150W color traces the Ly α break at $z \sim 10$, the F090W – F115W color is the best choice to investigate high-redshift sources at the epoch of reionization that peaks at $7.5 < z < 8$.

Our sample selection consisted of a photometric redshift selection and a color selection described in the main text. The photometric selection uses object coordinates from the JADES catalog. The WCS of our images is slightly different from those used by JADES. In addition, our images are slightly deeper than the JADES images, because we included images from programs other than JADES. Therefore, before applying the color selection, we refined the object photometry in F090W and F115W using our combined JWST images. We used `SEP`⁴⁵, a python version of `SExtractor`⁴⁶, to update the object coordinates using our F115W-band image. We extracted each source in a 21×21 pixel² 2D image cutout centered on its JADES coordinate. We then used the pixel peak coordinate (`xpeak`, `ypeak`) as the object coordinate because

¹<https://github.com/ceers/ceers-nircam>

²<https://stsci.app.box.com/s/1bymvf1lkrqbdn9rnkluzqk30e8o2bne>

our work focuses on the central AGN component. With the updated coordinates, we did photometry on the F090W and F115W band images using a circular aperture with $D = 0''.24$, which is robust for our faint point sources. For sources with multiple components in F115W that were not deblended by JADES, we identified their multiple centers and removed those that did not satisfy our selection criteria.

Image decomposition. Our image decomposition was performed in the F115W and F150W bands. The model consists of a point-source function (PSF) and a single Sérsic profile to model the point source and host galaxy. The method is developed from the literature^{27,47,48}, with a multi-band fitting code `GalfitM`⁴⁹. The PSF was constructed by stacking the point sources in each JWST field. For the galaxy component, we restricted the Sérsic index n to be less than 5, so our fitting tended to model the central component as a PSF component, leading to a conservative upper limit estimation.

In the fitting process, we first used the python codes `statmorph`⁵⁰ and `photutils`⁵¹ to estimate the position, morphology, and magnitudes for both point source and host galaxy components. The derived values were fed to `GalfitM` as input fitting parameters. The PSF position of each source was constrained to be within ± 1 pixel around its $(x_{\text{peak}}, y_{\text{peak}})$ to ensure that the PSF was fitted to the peak of our target. For the multi-component objects, the Sérsic positions were also limited to be within ± 1 pixel around their corresponding peaks. The magnitudes of the point source and host galaxy components were measured using the best-fit PSF model and the PSF-subtracted image, respectively. We performed two iterations of the `GalfitM` fitting to improve the fitting results. In the second iteration, we used the PSF-subtracted images to model the morphology of the host galaxy. We show two examples in Figure 2.

AGN UV LF. To construct the AGN UV LF, we first measured M_{1450} of the AGNs using their magnitudes in F115W and F150W. We derived k -corrections in the two bands as follows. For each band, we generated a grid of simulated quasars in the $[M_{1450}, z]$ space with $\Delta M_{1450} = 0.25$, $\Delta z = 0.05$. The quasar spectral energy distributions (SEDs) from ref.⁵² were designed to reproduce the colors of $\sim 60,000$ quasars. Assuming that the quasar SEDs do not evolve with redshift, we extended the model to redshifts $z > 7$. We further assume that the spectra blueward of $\text{Ly}\alpha$ was completely absorbed by the IGM. We used the simulated spectra to calculate the k -corrections as a function of redshift and luminosity. The k -corrections of the F115W and F150W magnitudes for an individual AGN were then interpolated from their grids, respectively. We calculated two values of M_{1450} based on the F115W and F150W magnitudes and adopted their average value as the final AGN M_{1450} for this AGN.

We also applied an alternative method to estimate M_{1450} . For each AGN, we calculated its flux at rest-frame 1285Å and 1835Å using the F115W and F150W magnitudes, where k -corrections were derived as previously described. We then fitted a power-law continuum to the flux and computed M_{1450} from the continuum. The resultant M_{1450} values agree well with those obtained from the first method. For simplicity, we used the average M_{1450} values from the first method for the following analyses.

We then estimated our sample completeness by computing a selection function as described in the main text. With the simulated F090W and F115W magnitudes, we added photometric errors using the standard procedure^{1,29}. Following the magnitude versus error diagram of the observed objects in the GOODS fields, we drew a large sample of simulated objects whose distribution in the magnitude versus error diagram is the same as that of the real objects. Note that the detection depth in the GOODS fields are not uniform because we combined many JWST images to take advantage of the available observations. Our procedure can properly handle this. The areas of GOODS-S and GOODS-N that we used are 67.0 arcmin² and 56.4 arcmin², respectively. The whole GOODS-N field and 25 arcmin² in GOODS-S field reach ~ 29.2 mag (5σ detection in a $D = 0''.24$ circular aperture) in F115W. The region of the other 42 arcmin² in GOODS-S is deeper (~ 30.1 mag). Finally, we calculated the fraction of sources in each M_{1450} and z bin that satisfied our color selection criteria. The UV LF was then constructed considering the

sample completeness. Table 1 lists our binned UV LF at $7.15 \leq z \leq 7.75$.

Tables

M_{1450}	ΔM_{1450}	$\log \Phi$	N
-19.41	1.7	4.31 ± 0.22	5
-18.20	0.7	4.71 ± 0.22	5
-17.50	0.7	5.13 ± 0.15	13
-16.80	0.7	5.38 ± 0.12	20
-16.10	0.7	5.73 ± 0.12	31
-15.35	0.8	5.89 ± 0.21	19

Table 1. Binned AGN UV LF. M_{1450} and ΔM_{1450} are the center and size of each magnitude bin. Φ is in units of $\text{Gpc}^{-3} \text{mag}^{-1}$. N represents the number of AGNs in each magnitude bin.

References (Continued)

44. Bagley, Micaela B. et al. CEERS Epoch 1 NIRCcam Imaging: Reduction Methods and Simulations Enabling Early JWST Science Results *Astrophys. J. Lett.* **946**, L12 (2023).
45. Barbary, Kyle et al. SEP: Source Extractor as a Library *The Journal of Open Source Software* **1**, 58 (2016).
46. Bertin, E. et al. SExtractor: Software for Source Extraction. *Astron. Astrophys. Suppl.* **117**, 393–404 (1996).
47. Sun, Wen et al. The Structure and Morphology of Galaxies during the Epoch of Reionization Revealed by JWST *Astrophys. J.* **960**, 104 (2024).
48. Chen, Chang-Hao et al. The Host Galaxy (If Any) of the Little Red Dots *arXiv e-prints* (2024).
49. Häußler, Boris et al. GALAPAGOS-2/GALFITM/GAMA - Multi-wavelength measurement of galaxy structure: Separating the properties of spheroid and disk components in modern surveys *Astron. Astrophys.* **664**, A92 (2022).
50. Rodriguez-Gomez, Vicente et al. The optical morphologies of galaxies in the IllustrisTNG simulation: a comparison to Pan-STARRS observations *Mon. Not. R. Astron. Soc.* **483**, 4140-4159 (2019).
51. Larry Bradley et al. astropy/photutils: 1.13.0 *Zenodo* (2024).
52. McGreer, Ian D. et al. THE $z = 5$ QUASAR LUMINOSITY FUNCTION FROM SDSS STRIPE 82 *Astrophys. J.* **768**, 105 (2013).